Slow-light regime and critical coupling in highly multimode corrugated waveguides

Hamza Kurt, Henri Benisty, T. Melo, Omer Khayam, Cyril Cambournac

Slow-light regime and critical coupling in highly multimode corrugated waveguides

H. Kurt,[1,2] H. Benisty,[1] T. Melo,[1] O. Khayam,[1,*] and C. Cambournac[1]

[1]*Laboratoire Charles Fabry de l' Institut d'Optique, CNRS, Université Paris-Sud Campus Polytechnique, RD 128, 91127 Palaiseau, France*

[2]*Currently at the Department of Electrical and Electronics Engineering, TOBB University of Economics and Technology, Ankara, 06560 Turkey*

**Corresponding author: omer.khayam@institutoptique.fr*

Received April 21, 2008; revised June 2, 2008; accepted June 6, 2008; posted June 23, 2008 (Doc. ID 95203); published July 30, 2008

Large and periodically corrugated optical waveguide structures are shown to possess specific modal regimes of slow-light propagation that are easily attainable. The very multimode nature of the coupling is studied by employing coupled-mode theory and the plane-wave expansion method. Given a large enough light cone, associated with a surrounding medium with low enough refractive index, we notably identify a critical slowdown regime with an interesting bandwidth-slowdown product. Essential features of these original systems are further explored: the nature of the coupled modes, the role of gain, symmetry effects, polarization, and relation with photonic-crystal systems. Practical systems are introduced using finite-difference time-domain methods, which provides first-order rules for the use of the above phenomena and their implementation in devices.

OCIS codes: 230.7370, 050.5298, 050.2770, 050.1940, 130.5296, 130.2790.

1. INTRODUCTION

Our contribution lies at the intersection of three topics: slow-light propagation, photonic-crystal optoelectronic devices, and mesoscopic optical systems. Our purpose is to bring new insights into the physics of light slowing down in corrugated optical systems and on its potential. We show theoretically that the slowdown effect is not restricted to tightly confined optical systems exhibiting only a few transverse modes, typically the so-called W1 and W2 photonic-crystal waveguides in the terminology of the photonic-crystal community (see p. 2). More precisely, our study reveals that a significant amount of the optical modes supported by a broad waveguide having a periodic corrugation on its sides can collectively lie in a slow-light regime. As is well known, the slow-light regime corresponds to flatband regions of the photonic dispersion diagram, arising at the edges of gaps or minigaps for any periodic system and not only for photonic crystals. A practical interest of our contribution is to point out that a slow-light behavior may be present even if only a wavelength-scale fraction of the broad waveguide width carries the longitudinal periodicity. This is at variance with systems such as photonic-crystal superprisms, whereby a slow dispersion of bulk photonic crystal is exploited in a selected arrangement. We hence point out the advent of collective slow-light behavior even in systems for which only a tiny fraction is periodic.

To complete this introduction, we relate our methods and systems to prominent ones of the related areas. The references for periodic waveguides in optoelectronics are distributed-feedback (DFB) lasers and the related distributed Bragg reflectors (DBR) [1–5]. Their description through coupled-mode theory (CMT) proved to be highly successful. Its most popular version involves the contradirectional coupling between a single forward-propagating mode and a single backward-propagating counterpart. Nevertheless, the extension of the coupled-mode formalism to (transverse) multimode systems has not been studied much [6]. We shall make use here of the coupled-wave formalism to describe the coupling between multiple forward and backward modes, focusing notably on the highly multimode case of large waveguides and the identification of critical coupling in such systems.

Our analysis is further substantiated with the plane-wave expansion (PWE) method and finite-difference time-domain (FDTD) simulations. Note that we shall sometimes call native or original eigenmodes the uncoupled modes, namely, the orthogonal guided modes of the unperturbed, i.e., noncorrugated, waveguide. For the corrugated waveguide, however, each guided mode has a nonzero overlap integral with the modulated region's useful Fourier component of the dielectric constant that reads $\Gamma \sim \int |E(x)|^2 \hat{\epsilon}(x) \mathrm{d}x$ [with $\hat{\epsilon}(x) = \mathrm{FT}[\epsilon(x,z)] = (2\pi)^{-1} \int \epsilon(x,z) \exp(iG_o z) \mathrm{d}z$ taken with the proper periodicity $\mathbf{G} = G_o z = (2\pi/\Lambda) z$; see Fig. 1(a)]. Through normalization, this overlap yields a key quantity for coupling. Uncoupled modes of slab guides can be found from textbooks [7,8], and are treated through their dispersion relations and/or their effective indices (see Appendix A). For thick slab guides, modes with the lowest effective indices are akin to Fabry-Perot modes. Then, the free spectral range (FSR) for a given angle, or equivalently for a given wave vector, is a convenient quantity to scale the band separation, a scaling that we shall retain for addressing the slow-mode regime as well.

Uncoupled modes also have underlying propagation

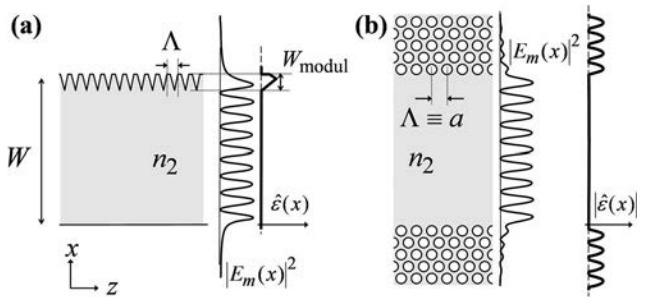

Fig. 1. (a) Generic broad waveguide with a side corrugation. The z-periodic dielectric component $\hat{\epsilon}(x)=\mathrm{FT}[\epsilon(x,z)]_{|G_0 z}$ is sketched together with the electric field profile $E_m(x)$ of a higher-order transverse mode. (b) The case of a photonic-crystal waveguide is similar, even though the cladding is extended.

angles, and this, importantly, enables depiction of the interaction with the corrugation as a diffraction event on a grating. This picture must nevertheless be handled with care since the diffracted wave next excites a waveguide, not the free space. As for photonic crystals (PhCs) and PhC waveguides [PhCWGs, as shown in Fig. 1(b)], they form a favorite playground for slow-light experiments. The common exact simulation tool for PhCWGs is the well-known PWE, whereby all mode fields are decomposed into their spatial harmonics (plane waves) [9–11].

Our group has pioneered the studies of multimode PhCWGs, for which we introduced CMT tools [12] and their application to mini-stopbands (MSBs) [13,14]. In this respect, a widely accepted labeling of PhCWGs is Wn for an n-missing-rows waveguide in this context. The special band diagram found in broad Wn PhCWGs [9,15] will appear, in this contribution, to reflect the effects of side corrugations, much as in DFB–DBR physics. To encompass both PhCWGs and more regular corrugated waveguides, our first approach is of the CMT type, based on multiple transverse uncoupled modes. To shift to realistic systems, we next study slabs with a triangular corrugation. We make use of the PWE method for the band structure as well as a FDTD model to substantiate actual slowdown effects in the multimode context. Not much can be said at the present stage about getting a simple impulse response, as the multimode complexity is not tamed in a generic numerical experiment. To summarize, our analysis resorts to three methods (CMT, PWE, and FDTD) and deals with fields in waveguides in five closely related fashions: uncoupled (native) and coupled modes (≡ bands) in the frequency domain; underlying plane waves in PWE; rays (~ underlying plane waves) in the diffraction picture—only for physical pictures—and electromagnetic fields in the time domain.

The paper is organized as follows. In Section 2 we give a simplified vision of the various periodic waveguides and we revisit, in a generic side-corrugated waveguide of width W, key quantities such as Γ, FSR, effective indices, and how they can be applied to PhCWGs. In this way, the reader is ready for presentation of the basic CMT model of Section 3. The results, notably the strong slowdown effect around a critical coupling regime, are discussed in Section 4. Section 5 provides a brief transmission and gain analysis (the most fundamental optical quantities affected by slowdown, beyond velocity itself, are gain and loss). An application to actual periodic waveguides (Section 6) is then developed thanks to PWE and FDTD. Conclusions are drawn in Section 7.

2. BROAD PERIODIC WAVEGUIDES

Generally speaking, once coupled-mode theory applies, the steps for calculating a waveguide's transmission matrix are (i) to determine the eigenvalues and eigenmodes $|E_{\mathrm{coupled}}\rangle$ on the basis of the uncoupled ones $|E_{\mathrm{uncoupled}}\rangle$; (ii) to calculate a generic transmission matrix $\mathbf{T}$ of the coupled modes for a propagation length L, of the form $\exp(\mathbf{A}L)$, where $\mathbf{A}$ is a diagonal matrix of eigenvalues; (iii) to calculate the product $\mathbf{P}^{-1}\exp(\mathbf{A}L)\mathbf{P}$ with the two input and output matrices connecting to uncoupled modes; and (iv) to apply the boundary conditions, e.g., to deduce a scattering matrix $\mathbf{S}$ giving the full modal transmission and reflection of any desired incoming uncoupled mode.

Broad waveguides lend themselves to our study if they exhibit a basis of several uncoupled (native) modes characterized by roughly equidistant branches. To show where this situation happens, we show in Appendix A the dispersion of a basic perfect-metallic-boundary slab waveguide of thickness W and index n_{core} treated within a scalar framework. Modal effective indices n_{eff} go down to zero in this ideal case. If, instead of the metal, we have a low-index uniform cladding n_{clad}, we have fewer allowed modes, since now $n_{\mathrm{eff}}>n_{\mathrm{clad}}$, i.e., modes are confined (here it means guided) only below the light line of the $(k_{\|},\omega)$ plane. This appears in Fig. 2(a) in the low-frequency region of the dispersion diagram. The number of guided modes $m_{\max}$ is controlled by the normalized width $\Lambda_c=2\pi W\lambda^{-1}(n_{\mathrm{core}}^2-n_{\mathrm{clad}}^2)^{1/2}$, essentially the upper bound of the $k_x W$ product. Note that all the higher-order modes are still approximately equidistant. However, for either metal or low-index cladding, the lowest-order guided modes (lowest effective indices) do not form nearly equidistant branches and hence do not lend themselves to our treatment.

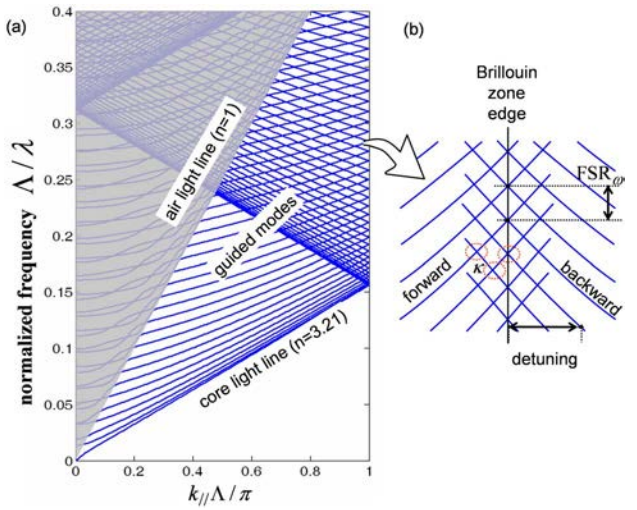

Fig. 2. (Color online) (a) Dispersion relation of a slab waveguide with artificial folding at the Brillouin zone edge. (b) Locally, branches of higher-order modes cross each other along a regular net and are equidistant. Their FSR is defined, as well as the phase detuning from the Bragg condition.

On such a basis, we now add along the waveguide a periodicity $\Lambda(\equiv a)$. The Bloch–Floquet theorem applies and a PWE of any packet of modes can be made, leading to the PWE modal modeling. This decomposition is not of direct interest to us, only the resulting bands are. A reference case is the empty lattice, periodicity being virtual [see Fig. 2(a)], for which the dispersion relations are artificially folded at the Brillouin zone edge. Crossings give rise to modal interactions and to anticrossings—opening of gaps and minigaps—as soon as the periodicity becomes real. The knowledge of actual bands by any method can thus be used to assess the strength of modal coupling through the size of local minigaps.

Let us now address somewhat realistic cases and have a look at the interplay of the guided mode field structure with the periodicity. Referring to Fig. 1(a), it is intuitive that CMT applies as soon as a mode, say, TE-polarized, of the type $E \equiv E_0 \sin(k_x x)\exp[i(k_{\|} z - \omega t)]$ has a modest overlap integral with the periodic region. More precisely, by depicting the periodicity map by the local amplitude of its useful Fourier-transform coefficient $[\epsilon(x,z) = \Sigma \hat{\epsilon}_p(x)\exp(2i\pi p/\Lambda z)$, where, here, only $p = \pm 1$ is of interest in addition to the mean local profile $\hat{\epsilon}_0(x)]$, the strength of the coupling constant $\kappa_{mm'}$ between a forward mode of order m and a backward mode of order m' is essentially dictated by the quantity $\Gamma_1(m,m') = \int E_m(x) E_{m'}(x) \hat{\epsilon}_1(x) \mathrm{d}x$ provided the fields are normalized.

Defining by W_{modul} the modulated region's thickness—where $\hat{\epsilon}_1(x) \neq 0$—the condition of a modest overlap, which is sufficient for CMT applicability, is essentially

$$\int_{\text{modulated region}} E_m(x) E_{m'}(x) \mathrm{d}x \leqslant W_{\mathrm{modul}} E_0^2 \ll W E_0^2. \quad (1)$$

This condition is usually satisfied in edge-emitting DFB laser diodes and similar semiconductor heterostructures vastly used for modulation or detection. The grating of a DFB laser is typically made by etching a 30–200 nm period grating in a layer well above the damage-sensitive active layer and by further burying it by regrowth: this leaves the modulation profile $\hat{\epsilon}_1(x)$ overlapping the tail of the mode. For a broad dielectric waveguide $W \gg \lambda/n_{\mathrm{core}}$, and Eq. (1) is then satisfied if $W_{\mathrm{modul}} \sim \lambda/n_{\mathrm{core}}$ or, in other words, if the corrugation is carried by a grating of wavelength scale also in terms of groove height.

Broad PhCWGs defined by n missing rows along a main PhC lattice direction also satisfy this condition when operated inside their bandgap. The physical reason, pictured in Fig. 1(b), is the strong decay of the modal field in the periodic PhC cladding. Strong refractive-index contrast is of course a crucial factor for this rapid decay, as it is for omnidirectionality of PhCs. For our purpose, it means that the integral appearing in $\Gamma_1(m,m')$ is sizable only in the first or second rows adjacent to the core. Thus, even though the cladding periodicity is unbounded for a PhCWG (W_{modul} is arbitrarily large), the inequality Eq. (1) holds and the CMT may apply among counterpropagating modes of broad PhC waveguides.

Previous work on CMT and PhCWGs has emphasized MSBs that arise among a fundamental mode $m = 1$ and a higher-order—Fabry-Pérot-like—mode ($m \sim m_{\max}$) [12–14]. This situation is not of direct interest here because the frequency spacing of the first few modes ($m \ll m_{\max}$) of a broad PhCWG (or a normal slab broad waveguide) varies quadratically, and not linearly, as a function of frequency.

Although not much studied to date, the transverse multimode general counterpart of the in-plane contradirectional coupling is interesting on its own, e.g., to circumvent power density issues and attain the ability to slow down a pulse with high absolute peak power, which seems delicate in the current studies on slowdown in ultimate systems of submicrometer width. Rosenblatt *et al.* [16] studied waveguide gratings to obtain resonant structures under certain circumstances. Ferrand *et al.* [17] studied porous-silicon-based broad modulated waveguide structures and reported features akin to MSBs, although the modulation was not of the PhC type. In Appendix B, we show from Eq. (1) why our regime leads to nearly constant interaction among modes, unlike other more familiar ones. In the zigzag ray picture of modes, this simply amounts to say that the grating's diffraction efficiency is weakly varying among a few adjacent modes. This regime of nearly constant interaction prompted us to consider a simple, essentially constant, intermodal coupling constant $\kappa_{mm'}$, as will be described in Section 3. Symmetry issues can help to better account for numerous real systems. For example, $\kappa_{mm'}$ can vanish for modes of opposite parity [versus x; see Fig. 3(b) below and [9] for considerations of the symmetry of PhCWGs].

The width dependence of coupling also appears in Eqs. (B1) and (B2) of Appendix B. For the lower-order modes, we have, for $\Gamma_1(m,m')$, the trend of the right-hand side of Eq. (B2), that is, $\kappa_{mm'} \propto W^{-3}$. Conversely, in the case of the m-independent situation of higher-order modes, only a W^{-1} dependence of $\kappa_{mm'}$, or $\Gamma_1(m,m')$, is found.

This specific feature, $\kappa \propto \Gamma \sim W^{-1}$, provides a simple general character to our study: since the frequency spacing of higher-order modes—the FSR at a given wave vector of a given angle—also scales like W^{-1}, we are able to describe a general multimode coupling situation by simply considering an identical coupling constant among modes, i.e., $\kappa_{mm'} = \kappa, \forall m, m'$, and by scanning the fundamental ratio

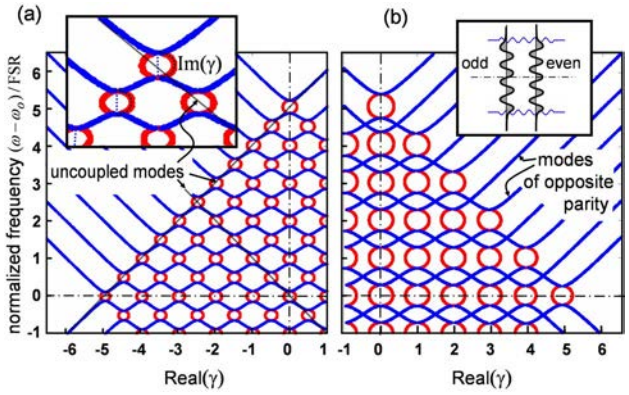

Fig. 3. (Color online) (a) Typical dispersion diagram for a coupling constant still small compared with the FSR. Blue, real part of the dispersion; red, imaginary part added to the real part (see inset). (b) Same as (a) for a case where parity (see inset) splits the interaction with the grating into two independent subsets, whose branches cross each other, thus doubling their frequency separation in the interaction region.

κ/FSR of our problem, i.e., essentially the ratio of mode interaction to mode separation. This ratio is profoundly dimensionless, either expressing the coupling constant κ (initially a wave vector) as a frequency, as is familiar to CMT practitioners, or using the uncoupled mode's group velocity the other way around to re-express the FSR (with some algebra based on Appendix A). A major consequence, not recognized until now, is that a broad corrugated waveguide with a given grating on its side can lead to light localization whatever its width W, provided that the grating is such that the ratio κ/FSR hits a critical region pointed out in this paper. Hence, a broad waveguide in which the periodic fraction W_{modul}/W is arbitrarily small can largely behave as a slow-light medium. It is the central motivation of this paper to shed more light on these effects from complementary viewpoints. It can be discussed how counterintuitive these effects are. For example, in their optical conductance analysis of a multimode system of the PhCWG type [18], Albaledejo *et al.* find that conductance scales just like the width for broader waveguides, without particular effects in the cases they investigate.

Finally, let us briefly complete the state-of-the-art started above [6,16]:

- Slow light in PhCs has motivated intense investigation in W1 membrane systems [19–21], but some studies tackled slow light in larger guides such as W2 and W3 [22,23]. Meanwhile, our group has also pioneered the use of MSBs and a kind of slow light for demultiplexing devices [14,24,25]. How much does our generic approach apply when reducing W (toward low mode numbers m) and thus violating the equidistant-mode assumption? It will be delicate to answer in an assertive manner at the present stage.
- Broad PhCWGs have been proposed for Littrow lasing [26]. The present study applies to them. The name Littrow was given because contradirectional zone-edge coupling induced by the PhCWG boundaries precisely corresponds to an elementary diffraction event in the usual Littrow mount of a grating (diffraction backscattering).
- Among non-PhC studies, two reveal few-mode flat-band structures partly reminiscent of our studies [27,28]. It is too early to provide a unified description of these systems with our approach.
- Codirectional coupling in multiwaveguide systems dates back to studies in [29]. They were also the object of intense attention recently in the presence of a transverse gradient across arrayed waveguides, in connection with fundamental phenomena such as Landau–Zener tunneling, optical Bloch oscillations [30–32], and nonlinear optics [33] in periodic structures.
- A last intermediate case is that of two adjacent waveguides with contradirectional evanescent coupling, in which case the supermode picture somehow amounts to a multimode description. But only a couple of modes are implied in total [6].

We purposely restrict here other developments toward nonlinear optics or light collection and detection applications to focus on the new modal and propagation features of our system. In Section 3, we exploit a canonical application of CMT with the interest of dealing only with the two main parameters: the constant mode separation $(\text{FSR})_\omega$ and the mode-independent coupling among them (κ). The later sections will confirm the relevance of several features found through the CMT, notably the existence of a critical coupling inducing a massive slowdown of light velocity and the appearance of two special dispersion branches above this critical value.

3. MULTIPLE EVENLY COUPLED MODES

We are interested in depicting a simplified version of Fig. 2(b), with all branches having identical slopes, instead of the slightly bent branches of actual modes in a slab waveguide. Let $a_n(z)$ and $b_n(z)$ represent the scalar local amplitude of the uncoupled forward (a) and backward (b) guided modes of order n along the waveguide, whereby we include the x dependence and the $\exp[i(\omega t \pm \beta_0 z)]$ factor of the electromagnetic field components. This may refer in practice to, e.g., TE modes, with a single transverse electric field component. $\beta_0 = \pi/\Lambda$ is the zone-edge wave vector [$\Lambda \equiv a$ is the lattice pitch in Fig. 1(b)]. The slope of a dispersion branch is depicted by $\beta_n = v_g \Delta\omega$, where β_n stands for the wave vector detuning from the Bragg condition, i.e., $\beta_n = k_\parallel^n - \beta_0$; $\Delta\omega = \omega(k_\parallel^n) - \omega(\beta_0)$ is the frequency detuning, and v_g is the group velocity. The uncoupled forward modes thus obey the simple evolution equation

$$-i\frac{da_n(z)}{dz} = \beta_n a_n. \tag{2a}$$

For equidistant modes [$\omega(\beta_0) = \omega_0 + \Delta n \times \text{FSR}_\omega$; see Appendix A and Fig. 2(b)] we have

$$\beta_n = v_g^{-1}[\omega - \omega_0 - \Delta n \times \text{FSR}_\omega]. \tag{2b}$$

Then, the basic coupled-mode equations among the $2N$ modes read as

$$\left(i\frac{d}{dz} + \beta_n\right)a_n(z) + \sum_{j=1}^{N} \kappa_{nj} b_j(z) = 0, \quad \text{with } 1 \leqslant n \leqslant N, \tag{2c}$$

$$\left(-i\frac{d}{dz} + \beta_n\right)b_n(z) + \sum_{j=1}^{N} \kappa_{nj} a_j(z) = 0, \quad \text{with } 1 \leqslant n \leqslant N. \tag{2d}$$

Material gain (g) and loss (α) parameters can also be included in these equations through an additional term that takes the net gain into account, i.e., after loss is subtracted from the gain.

The coupled evolution equations [Eqs. (2c) and (2d)] can be written in the matrix form

$$\frac{d}{dz}M = iCM, \tag{2e}$$

where M is a vector of $2N$ elements. It is ordered as $M^{\text{T}} = a_1, b_1, a_2, b_2, \ldots, a_N, b_N$, so that each 2×2 block along the diagonal is the usual single-mode CMT analysis. With our choice of M and $j = 1, \ldots, N$, we have $C_{2j-1,2j-1} = \beta_j$ (forward), $C_{2j,2j} = -\beta_j$ (backward), $C_{2j,2k} = C_{2j-1,2k-1} = 0$ if $j \neq k$

(no codirectional couplings), $C_{2j-1,2k}=\kappa$ (odd lines), and $C_{2j,2k-1}=-\kappa$ (even lines).

In this formulation, each forward-propagating mode interacts with all backward-propagating modes. However, in cases with a symmetry plane of the guide, for example, in the multimode PhCWG, parity effects take place (see, e.g., group theory considerations in [9]). This means, for example, that a forward-propagating even mode interacts only with all backward-propagating even modes and the same is true among odd modes. In this case, every other element in the series such as $C_{2j+1,2k}$ is set to zero. In the following, we refer to this as the symmetric waveguide case.

For each frequency of interest, we diagonalize the matrix C. We obtain eigenvalues $i\gamma$, which, written this way, are wave vectors with real part $\mathrm{Re}(\gamma)$ corresponding to propagating modes and imaginary part $\mathrm{Im}(\gamma)$ responsible for the evanescent modes in minigaps. We also obtain the eigenmodes $\{p_{jn}\}$, which are the coupled modes, as a linear combination of the underlying uncoupled (native) guided modes. The matrix $\mathbf{P}=\{p_{jn}\}$ is the matrix used to shift from one basis to the other and thus to project uncoupled modes onto the basis of coupled ones, e.g., for boundary conditions and incident flux definition. The degree of mixture will be a piece of information of some interest. One particular aspect that we shall examine is the partial norm of forward and backward components of an eigenmode, that is, the partial norm of the vectors $\{p_{2j-1,n}\}$ and $\{p_{2j,n}\}$ gathering all the forward and all the backward flows. We shall not need the full account of a Poynting vector at this stage. To situate the issue before the general discussion, we note that for two given counterpropagating modes, the coupling-induced splitting—2κ, the well-known textbook result—would be greater than the branch separation—FSR—for large coupling. This implies a regime of general mode interaction and calls for a profound analysis. To justify our simplistic model, it can also be intuited that in such a circumstance the knowledge of the details of the slow interbranch spacing evolution, i.e., when $\beta_n-\beta_{n-1}$ is not constant, turns out to be secondary.

4. RESULTS AND DISCUSSION

As a first step, the dispersion diagrams of a $2N$-mode weak coupling are investigated for a given κ. The FSR and group velocity are taken as unity without loss of generality. In Fig. 3(a) we essentially plot the dispersion diagram of the real part $\omega=\omega(k_\parallel)$. A few crossing gray lines represent the uncoupled-mode loci—slopes ±1 with unity separation, so that the vertical axis may be read directly as a normalized frequency $\bar{\omega}=[\omega-\omega(\beta_0)]/\mathrm{FSR}_\omega$—showing that they are similar to Fig. 2(b). Note that, in the figure, when the dispersion has an imaginary part, it is added to the real part and the color (see online) is changed, so that each minigap gives rise to two imaginary lobes of the dispersion diagram. More explicitly, we use as the abscissa $\mathrm{Re}(\gamma)+\mathrm{Im}(\gamma)$ instead of $\mathrm{Re}(\gamma)$ alone, and moreover, we change the color (see online) from blue to red when $\mathrm{Im}(\gamma)$ is nonzero (eigenmodes have an evanescent behavior, not due to the material losses but due to distributed feedback). The real part can generally easily be guessed as it lies midway between the two imaginary lobes (for zero material gain or absorption) and amounts to a vertical segment except at those more singular cases where upper and lower minigap edges substantially differ in terms of $\mathrm{Re}(\gamma)$.

In the example of Fig. 3(a), only $N=11$ basic modes are chosen, and a magnification is made (see inset) as the $2N=22$ branches have basic symmetries. The value $\kappa=0.15$—hence $\kappa/\mathrm{FSR}=0.15$—causes a sizable splitting, but still the overall picture is that the coupling is essentially the superposition of all elementary ones. The steepest local slope inside the net of curly branches appears to be diminished well below unity. The average separation of the bands in the interaction region is here $\Delta\bar{\omega}=0.5$, half the FSR, because of the twofold degeneracy lifting. From the basic $2\kappa=0.30$ splitting, it can be said naively that 60% of the room is forbidden between (anti)crossings and that the branch is substantially flattened. But this is not slow light yet, but only slower light, and significant dispersion oscillation remains.

In the example of Fig. 3(b), we display the effect of a symmetric layout (see inset). Correspondingly, the coupling becomes parity sensitive: even forward modes interact only with even backward modes, etc. To be consistent with the idea that this corresponds to a grating on both sides of a broad waveguide, the coupling constant is doubled, reaching $\kappa=0.30$. We notice that in the interaction region double branches are spaced by $\Delta\bar{\omega}=1$ instead of $\Delta\bar{\omega}=0.5$, as previously. Hence the branch pairs are really spaced by the original FSR, although the grouping (not exactly a degeneracy) now comes from symmetry effects rather than forward and backward propagation. The gap size is also roughly doubled. The degree of slowdown in this interaction region is thus similar: the steepest slopes are about similar to those in Fig. 3(a). Note that the pattern is reminiscent of broad PhCWG bands near the band edge.

Let us now increase the coupling strength from the weak to the strong coupling regime, that is, let us increase the dimensionless ratio $\kappa/\mathrm{FSR}_\omega$, with the idea that something happens when the splitting of $\sim 2\kappa$ reaches the same value as the separation FSR_ω. The coupling strength, and thus κ, can be tuned in real devices, for example, by varying the surface corrugation depth of a waveguide or by modifying the filling factor of the PhCWG in Fig. 1.

Our key findings are pictured in Figs. 4 and 5. We find that near $\kappa=0.32$ the band structure of Fig. 3(a) evolves to that of Fig. 4(a), here for $N=15$ modes. This pattern now

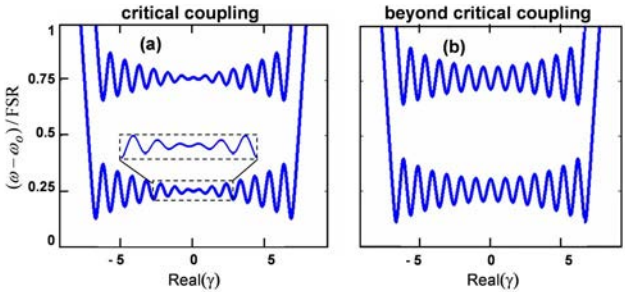

Fig. 4. (Color online) Lowest two bands of the positive frequency half-plane of Fig. 3(a) (a) at critical coupling and (b) above critical coupling.

exhibits a really flat region, especially near the center. The inset in Fig. 4(a) is a magnified view of the flatband around the origin. The oscillations are diminished and their amplitude vanishes at the center of the diagram. This observation is true for all the bands. This attainment of an extended slow-light regime, with a band completely constrained by minigaps, is generic and was checked empirically for several values of N. Also general is the fact that beyond the critical value κ_c of Fig. 4(a) the bands recover some oscillatory group velocity, as shown in Fig. 4(b) for $\kappa > \kappa_c$, therefore coming back to a situation generally similar to that of Fig. 3(a). Furthermore, as can be seen in Fig. 4(b), oscillation amplitude varies between the center and the sides of the interaction region. It is likely that this behavior originates from a kind of size effect: the oscillation amplitude at the edge is roughly independent of N, so that the oscillation amplitude variation vanishes asymptotically for large N, leading to arbitrarily large regions of slow group velocity within the present simplified assumptions. Since a good metric for slowdown phenomena is the bandwidth-slowdown product, this observation then indicates that the attainment of a large product only entails finding an unperturbed system exhibiting a sufficiently large region with linear equidistant branches around the Brillouin zone edge. In the limit case of the highest (or largest) slowdown in the center, we find that the generic relationship below holds (we leave its assessment to mathematicians, but we got approximately a 10^{-3} accuracy, $\kappa_c \approx 0.318$, in our case):

$$\frac{\pi \kappa_c}{\mathrm{FSR}_\omega} = 1.0. \tag{3}$$

If we take a closer look at the band structure, we see in Fig. 5 that passing through the critical coupling value highlights another particular feature. In Fig. 5(a), we plot the relationship between the imaginary wave vector $\mathrm{Im}(\gamma)$ and the coupling constant κ for the normalized frequency $\Delta\bar{\omega}=0.25$, that is, exactly in the middle of the flat branch nearest the reference frequency, pictured in the bottom of the Fig. 4 graphs. This branch is purely real until κ_c and $\mathrm{Im}(\gamma)=0$ in this range of coupling. Beyond κ_c, two imaginary branches appear in the plot of Fig. 5(b), and they gradually go to very large $\mathrm{Im}(\gamma)$. Figure 5(b) reveals the origin of these two new purely imaginary modes by plotting the band structure at $\kappa=0.4>\kappa_c$, with now the imaginary part, in red, being plotted as is, i.e., the abscissa is $\mathrm{Im}(\gamma)$—unlike Fig. 3, where $\mathrm{Re}(\gamma)+\mathrm{Im}(\gamma)$ was used as the abcissa to highlight the minigap structure: they clearly stem from the extreme real branches of our set.

These branches, unlike all others, are repelled and manifest a stronger anticrossing effect. We provide some more analysis later in Fig. 7. We may nevertheless readily state that these modes react through a collective response to the cumulated couplings rather than to a local response to a specific coupling. They hence pick up imaginary values in the gap that are much stronger than all the others. (This is a broad physical feature of coupled systems that we intend to comment on in further work, related in our view to the dark modes of multiemitter coherent systems.)

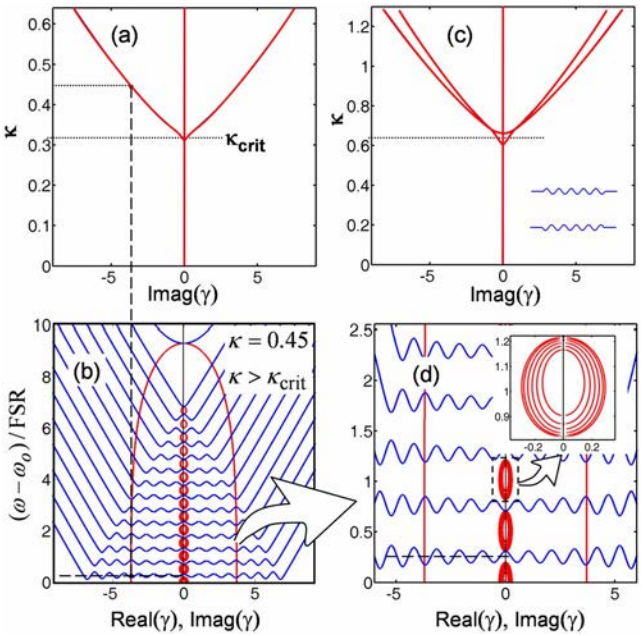

Fig. 5. (Color online) Imaginary eigenvalues for (a) a generic case for increasing the coupling constant up to $\kappa=0.6$. (b) Generic sketch of the band structure above the critical coupling with the two superlocalized states appearing with their high imaginary wave vector (all imaginary values are plotted with respect to the zero abscissa here); the dashed line shows the point used in (a). (c) Same as (a) but for the case of Fig. 3(b) where symmetry selection rules apply. (d) Enlarged band structure of (b) close to zero detuning. The inset shows that local stop bands are somewhat dispersed, as an effect of the finite number of modes.

Figure 5(d) shows a magnified view of Fig. 5(b), and its inset shows the set of the other imaginary branches among standard minigaps. It is seen that they form semicircles, much as they did for the subcritical cases ($\kappa < \kappa_c$). Other details of Fig. 4 are also similar, for example, the largest oscillation at the boundaries. Hence, the overall impression is that beyond the critical value, except for the two special modes, the situation reverts to the case of small coupling. This may explain why the critical case has not been observed previously or only marginally in 4×4 coupling cases: if one does not hit the critical value, bands that are not so flat are recovered. To finish this discussion, and to be consistent with Fig. 3(b), Fig. 5(c) shows what happens when parity effects modify coupling so as to split the ensemble of modes into two independent sets (the matrix C can be rearranged to form two $N\times N$ block-diagonal matrices in it): we have the same story twice; hence two superimaginary branches appear above the critical coupling. Due to the particular choice here of eight even modes and seven odd modes, the onset of the two families is slightly different and a local structure appears.

Let us come back to the slowdown effect itself, as in Fig. 4(a). To account quantitatively for this effect, we show in Fig. 6 a semilogarithmic plot of the group velocity of the first bands for three representative coupling values. One can see from the figure that, at the critical coupling [Fig. 6(b)], the smallest group-velocity oscillations take place with values that are an order of magnitude smaller than the other two cases. The exact slowdown performance depends on N in the present model and will in

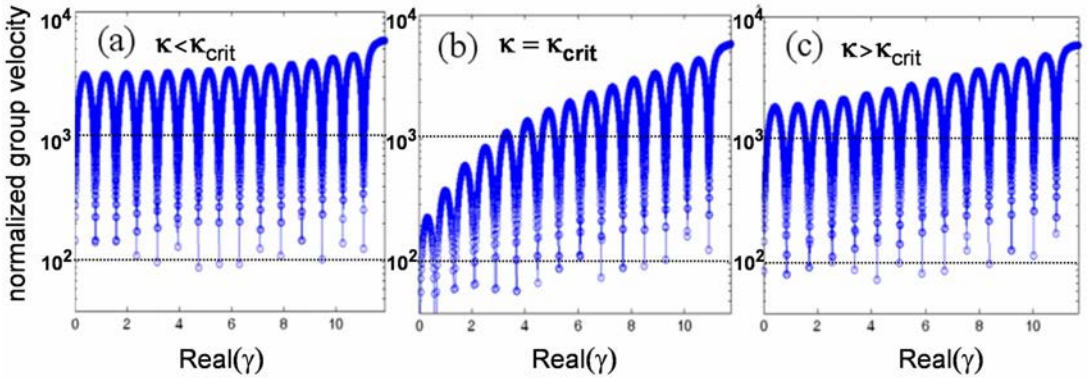

Fig. 6. (Color online) Semilog plots of the slopes of the first bands in Figs. 3(a) and 5 as a measure of group velocity, $|v_g|=|\partial\omega/\partial k_z|$, within a normalization factor. The three cases correspond to (a) below, (b) at, and (c) above the critical coupling. The order of magnitude of slowdown (around a decade) and its extent (spanning a few oscillations) are seen in (b).

practice depend on all the details of the dispersion. To situate how critical the coupling value is, let us mention that when the coupling constant deviates typically by 10% ($\kappa=0.28$ FSR or 0.34 FSR), the steep dip in the oscillations envelope in Fig. 6(b) at zero abscissa Re(γ) turns to a milder depression with a flat bottom spanning a couple of oscillations.

Here we may use the intrinsic simplicity of the CMT to track back the new eigenmodes in terms of the uncoupled waveguide modes. The first aspect is to check that the sign and value of the group velocity of a coupled-mode branch is related to a correspondingly larger weight of forward ($v_g>0$) or backward ($v_g<0$) modes ([10] explains the group-velocity additive properties with respect to the plane-wave components forming a Bloch mode). We checked this by using partial norms—defined as $\Sigma_j|p_{2j-1,n}|^2$ for forward modes and $\Sigma_j|p_{2j,n}|^2$ for backward modes. For example, if we investigate them along the same line $\Delta\bar{\omega}=0.25$ as in Fig. 5(b), these two weights manifest the expected advantage for, e.g., forward modes for positive slopes, and they get equilibrated for the low-group-velocity case, notably when approaching the critical point [branch center at critical coupling in Fig. 4(a)]. A more detailed analysis provides some insight into the appearance of the two special modes. Figure 7(a) shows the dispersion in this same region $\Delta\bar{\omega}=0.25$ for three coupling values below and above κ_c, and at κ_c. The modes pointed out by the three arrows in the three subplots of Fig. 7(a) have a decomposition $p_{j,n}$ that we render into Figs. 7(b)–7(e) as indicated. Two colors (see online) are used to plot the real part of the amplitudes Re($p_{2j,n}$), Re($p_{2j+1,n}$) (odd indices for forward modes, even ones for backward modes). Ignoring the complex part is a simplification, as the marked trends we are going to show are modestly mitigated by the imaginary part. The case in Fig. 7(b) is a case below critical coupling. It shows that the decomposition is rather pure, i.e., with a largely predominant term, $j=8$ here. It is specifically the backward $j=8$ mode for the negative Re(γ) value pointed in Fig. 7(b): the symmetric positive Re(γ) value just yields the $j=8$ forward mode as the dominant one instead, but it has exactly the same amplitude and one is hidden below the other in our plot conventions, using the same abcissae j for forward and backward modes Around κ_c, the distribution starts to spread around the central $j=8$, and a strong admixture of forward and backward modes occurs, as expected for very stationary modes. Above κ_c, the modes of the real branches [Fig. 7(d)] are much like those of Fig. 7(b), whereas the two special modes with large imaginary parts, whose distribution is shown in Fig. 7(e), acquire a really broad decomposition over all uncoupled modes,

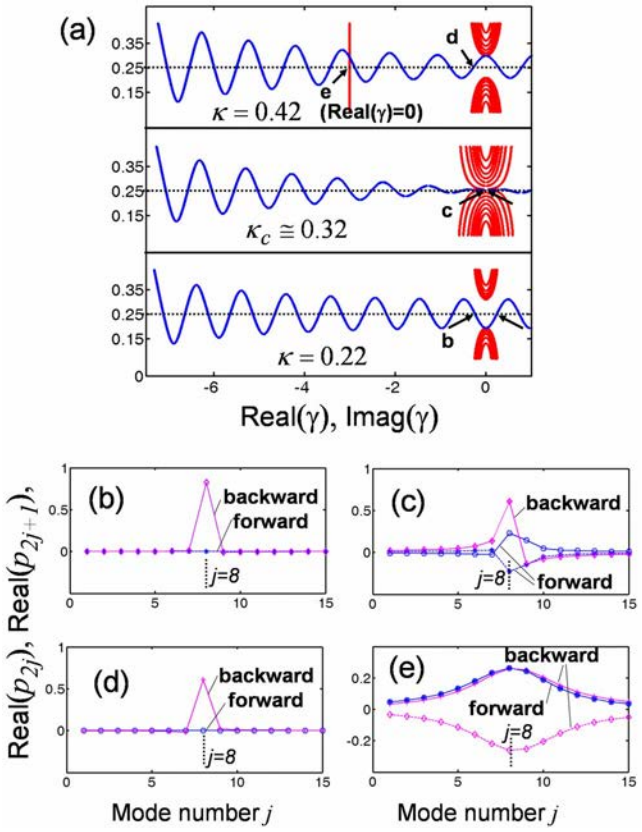

Fig. 7. (Color online) Study of eigenmode decomposition: (a) the branches associated with selected coupling constants and the points b–e chosen for the plots below. (b) Real part of the forward (blue) and backward (magenta) coefficients for the modes near the origin. The two modes give the same distribution, with just backward and forward swapped. An imaginary part also exists, with rather more mode mixing, but no large coefficients. (c) Appearance of more mixing near critical coupling. (d) Disappearance of the latter strong mixing above the critical coupling. (e) Strongly mixed nature of the superimaginary modes above critical coupling.

with odd or even parities in the decomposition, according to the sign of $\mathrm{Im}(\gamma)$. This situation is physically consistent: special modes can gather a large imaginary value only by coherently concentrating the coupling strength from all the other modes. However, the decomposition of all the other Bloch modes for which $|v_g|$ gently increases beyond κ_c retain the simple almost singly peaked distribution they had below κ_c.

A deeper analysis will be needed in future work to understand the nature of optical Bloch (=coupled) modes in these systems well. This aspect is at the root of an apparent paradox: if one forgets the Bloch nature of modes in a DBR and only thinks in terms of successive Fresnel reflections, then transmission would always be impeded and there would be no bands, only gaps. Here, we can think of a ray impinging at adequate incidence on the side corrugation and undergoing a diffraction event in Littrow or near-Littrow geometry [26]. At each bounce, only a fraction of the light goes forward, so that naively, only backscattering is possible for a long enough system [26]. The formation of bands allows this paradox to be solved: eigenmodes (Bloch modes) acquire forward and backward components everywhere, and transmission windows (bands) are retained. What we find here is the critical coupling situation whereby bands are maximally squeezed and transmission is almost always impeded, save for very narrow minibands.

The current analysis has clearly identified the occurrence of a genuine slow-light regime in these broad corrugated waveguides. The plots of Figs. 4 and 6, however, suggest that its extent in the dispersion diagram is limited. We can therefore think of designs providing even more uniformly flat bands by engineering the complex dispersion diagrams. We attempted, for example, to introduce a small extra variation of the coupling constant, whereby κ_{nj} is varied linearly or quadratically away from the central n_0 mode, instead of the constant value taken before. We could find, under these conditions, ultraflat bands that feature low group velocity on an extended range compared with Fig. 6(b), for example. Such a slow variation of coupling is akin to the slow variations of diffraction efficiency in gratings. Details of slowdown performance management are, however, out of the scope of the present paper in which we rather focus on the very concept and its basic derivations.

5. TRANSMISSION AND GAIN ANALYSIS

The use of these broad corrugated waveguides for transmission of signals gives a more practical view of their potential and also gives us the opportunity to consider the case of an active medium, with gain, acting more or less like a DFB laser [26]. Considering a corrugated waveguide of length L, from $z=0$ to $z=L$, we are interested in the situation defined by a single uncoupled mode of order $n=n_0$, e.g., the central mode of our uncoupled branches, impinging on this section in the forward direction. The boundary conditions for the forward and backward waves become $a_n(0)=\delta_{n,n_0}$ and $b_n(L)=0$. The transmission and reflection coefficients, integrated over all modes, can be obtained for this normalized excitation simply as follows:

$$T(\omega)=\sum_{n=1}^{N}|a_n(z=L)|^2, \tag{4a}$$

$$R(\omega)=\sum_{n=1}^{N}|b_n(z=0)|^2. \tag{4b}$$

In Fig. 8, we show the spectral transmission and reflection coefficients when only $a_{n_0}(0)=1.0$ is excited for two representative κ values.

We show the result for two representative κ values and detail only the spectrum of the narrow miniband nearest the origin. When coupling is subcritical, the situation is reminiscent of light transmission through one-dimensional Bragg stacks: outside the miniband, transmission is strongly suppressed, whereas within the miniband there are four well-behaved sharp peaks (this is related to the value of the κL product). The situation at critical coupling gives rise to extremely squeezed peaks and is so singular that we defer detailed analysis to a further study. Beyond critical coupling there are again four prominent peaks but with additional secondary peaks. Furthermore, unity transmission is no longer reached in this supercritical regime. We attribute this effect, and the increased spectral complexity, to the more demanding coupling condition of the eigenmodes beyond critical coupling.

Using a similar procedure we can get the transmission and reflection gain coefficients if gain is added to the former passive structure of length L. One common way of presenting $T(\omega,g)$ and $R(\omega,g)$ is to display them in terms of contour plots as in [5]. The diverging points correspond to the threshold gain for the corresponding modes. Modes with frequencies closer to the bandgap have lower thresh-

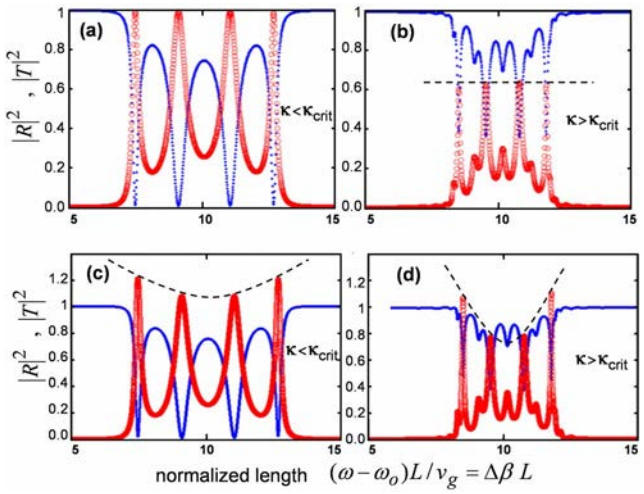

Fig. 8. (Color online) Study of transmission along a section of given length L, without or with gain. Here, one of the higher-lying interacting bands is studied. (a) Peaks spanning a transmission window defined by the band limits are similar to those of a 1D DBR for a low coupling constant. (b) For a coupling constant above the critical value, a complex pattern occurs, with transmission peaks not reaching unity. (c) In the presence of gain, the narrower peaks associated with the slower local group velocities have the larger gain. (d) Same effect for a large coupling constant, with more contrast as some peaks are quite narrow. The dashed curve is a guide to the eye.

old gain and are amplified first in a device. Lower threshold gain should therefore result from approaching the critical coupling (low group velocity, flatbands). Figures 8(c) and 8(d) show the transmission and reflection coefficients under small-gain condition ($gL=0.01$) in the same two coupling cases as in Figs. 8(a) and 8(b). As expected, due to gain, transmission and reflection coefficients may exceed unity at resonant peaks. The peaks are narrower for the supercritical case. The zero-gain peak value was smaller (below unity, as stressed above), so that if we look at the differential gain the narrower peaks have a higher differential gain. It is just because we stuck to the small-gain regime that the peak gains are not higher than in the subcritical case; with some more gain they would catch up and eventually ensure lower threshold gain under adequate conditions. At critical coupling, again a modal detailed study of the singularity is requested. In our attempts, we did readily observe an order of magnitude larger peak differential gain under the critical coupling condition (gain in transmission of over 10 instead of 1.2 in Fig. 8, for the same bulk gain). The overall picture is the increase of peak differential gain as an inverse function of the group velocity. This picture notably holds at and above the critical coupling, in spite of the extra complexity of this condition.

6. APPLICATION TO ACTUAL PERIODIC WAVEGUIDES

To validate the observations resulting from CMT, an exact analysis based on PWE is further carried out. First, 1D broad waveguides are provided with a triangular corrugation of height h along the top of the guide (Fig. 9). This choice of a triangular corrugation naturally provides larger diffraction efficiencies around the Littrow condition, much more than a rectangular profile. We shall use the dimensionless parameter h/Λ, and we restrict ourselves to $h/\Lambda \ll W/\Lambda$, which is in agreement with the arguments exposed in the introduction—here h/Λ will not exceed 2.0. The two outer media are air and the guide medium has a refractive index of $n_2=3.21$—typically that of InP and related compounds. The parameters are defined in Fig. 9. The figure also shows, in view of the FDTD simulations, the local plane-wave exciter we used, making an angle θ (=33°) between the wave front and the guide propagation axis ($\theta \to \pi/2$ for the fundamental mode). For

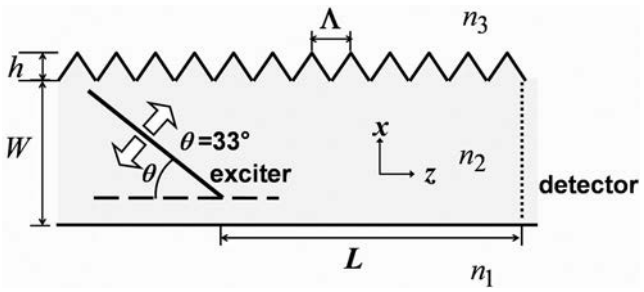

Fig. 9. Real broad periodic waveguide with triangular corrugation for studies by PWE (band structure) and by FDTD (propagation). Indices are $n_1=n_3=1$ and $n_2=3.21$ in our case.

the PWE study that is presented, first, we use a supercell of width $2W$ along transverse dimension x. The large majority of confined modes below the light line modes in the air are not influenced by this artificial boundary since they are evanescent in the air. Only modes above the light cone propagate in the air and see the supercell boundary condition along x.

Figure 10 is the band structure—real and imaginary as in Fig. 3—obtained using a supercell for $h/\Lambda=1.0$ and the width $W/\Lambda=15$. Much as in Fig. 2, there are guided modes that fold at the Brillouin zone edge, i.e., at $k\Lambda=\pi$, and they mutually interact. From an optics viewpoint, sketching the guided mode as a zigzag ray, this Brillouin zone condition is nothing but the Littrow diffraction condition onto the grating, yielding backreflection (see [26]). Therefore, the diffraction efficiency in this Littrow or near-Littrow configuration provides another approach to understanding the variation of the coupling coefficient.

In Fig. 10(b) the slow-light region is essentially located inside the curly braces. We can see that the bands really flatten out, across several FSRs vertically and across several anticrossings horizontally, as already highlighted by CMT. A magnification on the sole real bands is provided in Fig. 10(c), showing that a group index $n_g=c/v_g$ on the order of 50 holds for the large majority of the bands in the slowdown region. Two features are worth a comment.

First, the dispersion relation of these flat regions actually borrows an overall parabolic shape, much as a Fabry–Perot mode, but with the center around $k\Lambda=\pi$ instead of 0. This is probably a profound limit; our system cannot be substantially slower than a Fabry–Perot of similar width would be. Still, it is here equivalent to the situation of a metallic guide, since waves are not lost upon their residual z propagation. Hence, this situation is a novel combination of slowdown and propagation capability, making the physics of perfect ideal metallic waveguides partly accessible to dielectrics and optical frequencies.

Second, the new special modes and their two imaginary branches of Fig. 5(a), which look like a mathematical consequence of the simplification of the CMT, are now seen to exist also through this PWE analysis. They appear somewhat more gradually, but they are clearly seen. We intend to achieve their detailed study in further work, notably to investigate whether they could offer a realistic opportunity for stronger localization than other modes thanks to their faster imaginary decay.

A further analysis aiming at generalizing our results to different corrugation heights h is presented in Fig. 11. We first sketch in Fig. 11(a) the generic miniband pattern at and around the slowdown region and notably how extrema of the spacing $\Delta\omega(k_\parallel)$ are arranged between adjacent bands [$\Delta\omega(k_\parallel)=\omega_{n+1}(k_\parallel)-\omega_n(k_\parallel)$, where $k_\parallel \equiv k_z$]. It is seen that if one tracks an extremum vertically between adjacent bands, two situations (red and blue, see online) arise. Around a band there is a maximum on one side and a minimum on the other side. From low to high frequencies, for example, if a maximum is chosen to start with, it will diminish, whereas on the other side of the same band, there is a minimum that grows when incrementing the band index. Hence there will be a crossing of the two difference functions $\max[\Delta\omega(k_\parallel)]$, $\min[\Delta\omega(k_\parallel)]$ associated

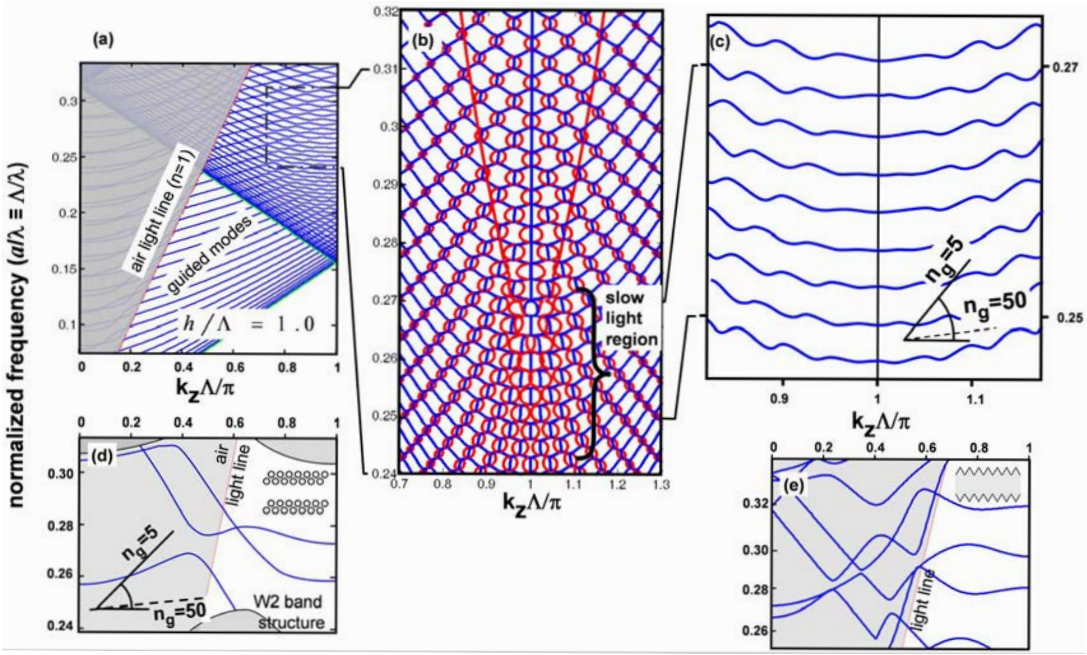

Fig. 10. (Color online) (a) Bands of the system illustrated in Fig. 9 (*E* polarization), with $h/\Lambda=1.0$ and $W/\Lambda=15$. (b) First magnification of the dotted box, with real and imaginary dispersion [same convention as Fig. 3(a)], showing the superimaginary modes. (c) Second magnification of the real dispersion only, highlighting the low group-velocity range attained, $v_g=c/n_g$. (d) Band structure of the W2 photonic-crystal waveguide, showing slow modes of appreciable bandwidth. (d) Band structure of a corrugated guide with $h/\Lambda=1.0$ on both sides and $W/\Lambda=1.5$ for comparison.

with band pairs, i.e., a crossing of the vertical size of the blue and red (see online) arrows of Fig. 11(a) Of course, local extrema near $k\Lambda=\pi$ are the best suited for this study.

A plot showing the two extremum functions $\max[\Delta\omega(k_\parallel)]$, $\min[\Delta\omega(k_\parallel)]$ is illustrated in Fig. 11(b), whereby the crossing is seen to happen a little below the normalized frequency $\omega\Lambda/2\pi c=\Lambda/\lambda=0.25$. Because the crossing of the two curves evidences a locally linear behavior, it is clear that the oscillations of the bands for frequencies above or below the crossing possess mean group velocities $\langle|v_g|\rangle$ that increase linearly as indicated by the gray "butterfly" depicted around the crossing. It is then a matter of taste, without a further prescription, to define the boundary of the slow-light region. The trend seen here can be associated with that of Fig. 6. The dip in overall group velocity was seen along a band in the central plot of Fig. 6. What is revealed here is the trend across several bands. It arises because the coupling coefficient cannot be critical for all frequencies. There is no reason for such a feature for the nonspecific grating shape that we have selected, whose diffraction efficiency is expected to vary without special features at the angles and frequencies of interest.

The crossing point evolution for different corrugation heights $h/\Lambda\neq 1$ is depicted by the dotted curve. It goes to lower frequencies for more corrugated structures and vice versa. We plot the loci of the slow-light regions in Fig. 11(c). We point by ellipses the crossing region of graphs similar to Fig. 11(b), but obtained for other corrugation heights. The result is a gently increasing curve toward low frequency and large corrugation. Note that, at the lower corrugation and higher frequencies, another region appears, indicated by lozenges. The usefulness of this secondary slow-light region is, however, limited in practice because there is little room left below the light line, since the air light line meets the band edge and closes the guided mode region a little only above $\omega\Lambda/2\pi c=\Lambda/\lambda=0.4$.

Similar trends hold for doubly corrugated systems (one grating on each side). The trends are then modified much as the difference between Fig. 3(a) and 3(b). Extension to PhCWGs is not completely straightforward. The usual variable parameter of a PhCWG is the air-filling factor of the triangular lattice of holes. It affects both the bandgap position, hence making it possible to lose confinement, and the corrugation's effective height or, in other words the diffraction efficiency, as we discussed in [26]. In practice, if one retains PhC claddings that are unmodified and that consist of circular air holes in a triangular arrangement, there are only small regions of the TM polarization, i.e., **E** along the hole axis, where we could spot flatband regions. This explains that in spite of a high interest that has been directed toward multimode PhCWGs, including for slow light and related phenomena [23,24,34], no actual strong systematic flattening of the kind reported here has been noticed.

Let us briefly discuss the narrow width limit. Our initial assumption of a broad waveguide, as prompted by [26] in the case of a W31 PhCWG, exploited the feature of equidistant modes, which was explicit in the CMT approach. In addition to our claim on slowdown and critical coupling in CMT, the data in Fig. 11 indicate that this phenomenon takes place in a real system for a particular corrugation strength, thus forming a demonstration of a critical diffraction efficiency in near-Littrow geometry, leading to the hyperbola-shaped regions of Fig. 11(c).

Upon reducing the waveguide width, however, the modal equidistance is increasingly relaxed and subse-

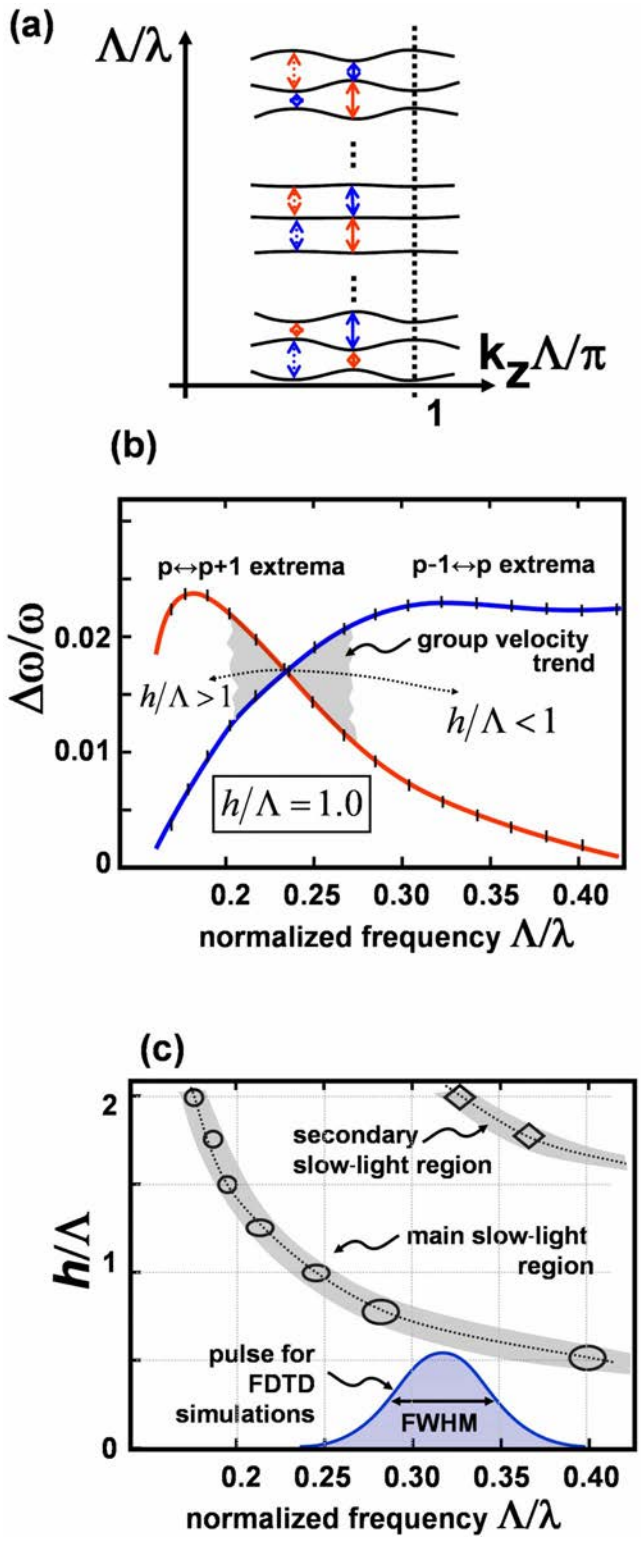

Fig. 11. (Color online) (a) Analysis of flatbands around extrema of minibands and minigaps. Red/blue spacings increase/decrease along a vertical. (b) Plot of the extrema among two adjacent bands (for $h/\Lambda=1.0$) as a function of band frequency. The crossing is the flatband situation. Vertical dashes indicate the miniband location for $W/\Lambda=6$. $|v_g|$ follows the trend of the gray "butterfly," linear versus $(\omega-\omega_o)$. The crossing point evolves along the dotted curve for variable h. (c) Slow-light regions, primary and secondary, as deduced from a study at various corrugation heights (ellipses and lozenges). The Gaussian is the spectrum of the source pulse used for FDTD simulations in Fig. 12.

quently the slowness feature is concentrated on a lesser number of guided modes. Ultimately, the critical diffraction efficiency no longer holds for a remaining single mode, unless it hits the right Littrow angle at the right frequency. This adds a selection rule that broad waveguides could naturally satisfy for at least a few modes because of the extension of the slowdown region. Because slowdown is so intensively studied in narrow PhC waveguides, Fig. 10(d) recalls the typical case of the W2 dispersion relation after [23] showing group indices up to $n_g=c/v_g\sim 25$. To provide a useful comparison, we devised that a guide with the same triangular corrugation depth $h/\Lambda=1.0$ implemented symmetrically for consistency with the PhCWGs in general, but a narrow width $W/\Lambda\cong 1.5$, would satisfy slowdown conditions in almost the same frequency region. This is indeed the case, as shown in Fig. 10(e). The modes near the band edge show a slowdown of the order of $n_g\sim 50$ comparable with that of Fig. 10(c), and rather better than the W2 case of Fig. 10(d) [35].

Finally, to picture the explicit effect of the slow-light regime, electromagnetic-field propagation through broad corrugated waveguides ($W/\Lambda=6$) is investigated by employing FDTD under different corrugation depths. The role of the corrugation depth to slow down the electromagnetic field is naturally analyzed by taking the field propagation through a noncorrugated waveguide as a reference. A broad modulated Gaussian pulse centered at the normalized frequency $a/\lambda=0.32$ with FWHM of 0.075 is launched with an incident angle of 33° off the z axis (wave front at 33° with the x axis) as shown in Fig. 9. Figure 11(c) gives the anticipated flatband regions. We chose here to select three canonical corrugation depths $h/\Lambda=0.5$, 1.0, and 2.0. The broad bandwidth of the pulse will result in some part of the light being delayed more than the other, hence leading to giant pulse broadening.

As can be seen, the input source spectrum overlaps rather well with the slow-light regions of the 0.5 and 2.0 corrugation depths and falls somewhat more aside for the corrugation depth of 1.0. The width of the beam, also Gaussian, is approximately $w=11\Lambda$, in order to minimize diffraction-induced spreading and to hit well-defined wave vectors as much as allowed by the physical guide width. The length of the waveguide L from the source center to the sensor is $L=50\Lambda$, and the field propagating along the positive z direction is stored in time at the outside of the waveguide along its cross section (shown as a dotted line in Fig. 9). The field propagating along the opposite direction is allowed to travel over long enough distances to suppress the temporal appearance of the backreflection of the field at the opposite end of the waveguide (but not the corrugation-induced reflection along the guide, of course). The field detection is continued for a total time step of 80,000 periods, corresponding to approximately 100 ps for a standard wavelength of 1 μm.

Figures 12(a)–12(d) show the field power summed along the cross section of the waveguide. In the reference case of Fig. 12(a) there is no corrugation at all. For the three other cases shown in Figs. 12(b)–12(d), h/Λ is set to 0.5, 1.0, and 2.0, respectively. It can be seen that by contrast to Fig. 12(a), all three cases lead to large delays (note also the changes in vertical scale). This delay is

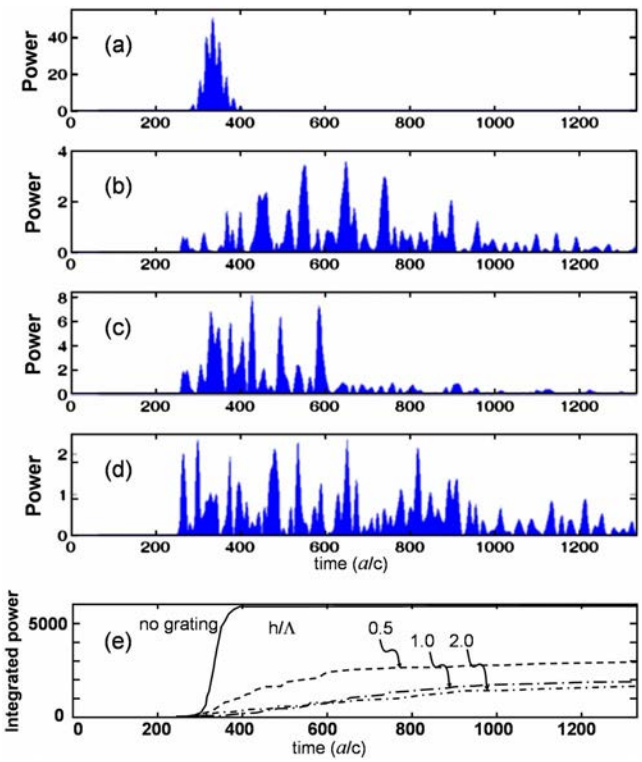

Fig. 12. (Color online) FDTD observation of light slowdown for waveguides with $W/\Lambda=6$ and variable corrugation depth. (a)–(d) Output power integrated along the cross section (see Fig. 9) and plotted as a function of simulation time. (e) Plot of cumulated signals showing the slower rise time. The corrugation depths h/Λ are indicated. Cases (b) and (d) give the flattest rising edge, in agreement with the degree of coincidence of the pulse spectrum with the critical regions in Fig. 11(c).

clearly more pronounced for the two extreme cases [Figs. 12(b) and 12(d)], while it is relatively weak for Fig. 12(c). In Figs. 12(b) and 12(d) the flatbands strongly slow down the power flow in the time domain. These cases are still generic and much more work is needed to clarify how focused in frequency and wave vector an input pulse needs to be to take advantage of the ~100-fold reduction, as expected from Fig. 6. We will report elsewhere how we may turn a band diagram into a delay analysis for the setup considered here.

A simple synthetic quantification can be made, as shown in Fig. 12(e): the cumulated powers, i.e., the energy acquired by integrating over time the Poynting vector flow at the guide exit is given. It further supports the impression that the extreme cases are the slowest ones. The jagged aspect of Figs. 12(b)–12(d) is absent in this plot, so that, if this comparison could be made with experimental data, we would doubtlessly recommend it, rather than tracking the full time pattern of an ultrashort pulse. The main conclusion to retain from this last section is that we have clearly evidenced, in the time domain as well as in the frequency domain through the band structure, that by engineering the corrugation depth, i.e., the coupling coefficient among the waveguide multiple modes, slow-light propagation can be attained with a factor of 10 easily at hand. Although delay dispersion can still be a matter of discussion, the simplicity of the layout able to produce these delays is remarkable and would not have been intuited from a pure geometrical diffraction approach, as such an approach would have predicted a virtual absence of light due to successive irreversible backscattering events.

7. CONCLUSIONS

We have pointed out a hitherto unnoticed property of multimode corrugated waveguides: they are able to provide a slow-light propagation regime under the appropriate waveguide parameters—ratios of waveguide width and corrugation depth to periodicity of the corrugation—in a sizable fraction of their dispersion diagram. The underlying physical mechanism is a Bragg feedback that can also be analyzed as a Littrow-type backdiffraction effect combined with the waveguide discretization constraints. A phenomenological and generic study exploiting coupled-mode formalism for both bands and gaps highlighted the prominent role of coupling strength. A critical coupling condition was identified that produced ultraflat bands. The flatness can be made arbitrarily low in coupled-mode theory over several successive crossings. The persistence of slow modes shows the relevance of the Bloch-mode picture, as light would be simply decaying upon propagation in the naive grating diffraction picture ignoring the profound physics of guided waves. As for the attainment of the critical coupling in a real system, it was clearly evidenced in modeling realistic systems, such as corrugated slabs of index $n=3.21$, with a top triangular corrugation of limited depth ($\sim\lambda/n$). A more explicit view of the effect of low group velocity and of the critical coupling was investigated thanks to the FDTD method, and the trends were confirmed by an original comparison of the FDTD delayed propagation results with the group-velocity distribution of excited modes. Applications exploiting a mere corrugated waveguide have the interest of simplicity and of possible tuning and transduction action at the accessible grating surface. As for a photonic-crystal version, it would likely demand more complex shapes than round holes, but one could gain from the omnidirectional bandgap access to angular windows in the guide that are incompatible with total internal reflection. Applications of broad photonic-crystal waveguides to produce original Littrow lasing systems was recently reported by our group [26]. The present study, detailing a blend of simple and more complex physics, suggests that highly multimode waveguides have an interesting potential to hit a variety of conditions implementing enhanced light-matter interaction, that, to date, were reported almost exclusively around ultimately confined systems (waveguides or microcavities).

APPENDIX A

We start from the standard relation of the mth order mode dispersion for a waveguide of width W, index n_{core}, with perfect metal boundaries:

$$\left(n_{\text{core}}\frac{\omega}{c}\right)^2 = k_{\parallel}^2 + m^2\frac{\pi^2}{W^2}. \tag{A1}$$

We develop it around any particular wave vector value $k_\parallel^0$, associated with a frequency ω_M^0 and a mode order M: $k_\parallel = k_\parallel^0 + \Delta k_\parallel$ and $m = M + \Delta m$ ($k_\parallel^0$ can be the Brillouin zone edge, $k_\parallel^0 = \pi/\Lambda$, but this particular case is not needed here). Dropping the square of the smaller $\Delta k_\parallel$ and Δm terms and using standard square-root approximation, we get

$$\frac{n_{\text{core}}}{c}\omega \cong \frac{n_{\text{core}}}{c}\omega_M^0\left[1 + \left(\frac{c}{n_{\text{core}}\omega_M^0}\right)^2 k_\parallel^0 \Delta k_\parallel + \left(\frac{c\pi}{n_{\text{core}}\omega_M^0 W}\right)^2 M\Delta m\right]. \tag{A2}$$

This is a bilinear form in $\Delta k_\parallel$ and Δm. This essentially justifies equally spaced dispersion branches, with identical slopes. To better relate the parameters to practical ones, one can use either the effective index $n_{\text{eff}} = ck_\parallel^0/\omega$ or the angle of the underlying ray in the guiding medium, defined by $\sin(\theta) = ck_\parallel^0/(n_{\text{core}}\omega)$ (θ is the angle of mode M at frequency ω_M^0). This is more instructive and yields the alternative form

$$\omega \cong \omega_M^0\left[1 + \sin^2(\theta)\left(\frac{\Delta k_\parallel}{k_\parallel^0}\right) + \cos^2(\theta)\left(\frac{\Delta m}{M}\right)\right]. \tag{A3}$$

In this form, the free spectral range is pretty obvious, $\text{FSR}_\omega = \omega_M^0 \cos^2(\theta)/M$, as well as the group velocity, $v_g = \omega_M^0 \sin^2(\theta)/k_\parallel^0$. One more step is to obtain a dimensionless version by using FSR_ω as the frequency unit, which amounts to shifting dispersion relations by unity among the branches. The wave-vector term of the equation is then naturally factorized with the waveguide width W. Namely, more algebra yields the identity

$$\frac{\omega - \omega_M^0}{\text{FSR}_\omega} \cong \Delta m + \left[\frac{W}{\pi}\tan(\theta)\right]\Delta k_\parallel, \tag{A4}$$

where the dimensionless frequency and wave-vector quantities are related by a mere $\tan(\theta)$ term having the formal role of 1/(group velocity). This ratio is typically on the order of unity in realistic systems (45° modes).

APPENDIX B

To unify as much as possible these systems, it is worth recalling basic scaling rules for the coupling strength $\kappa_{mm'} \propto \Gamma_1(m,m')$ when the modulation lies on the edge of the guide, as is most common in optoelectronics. For the lower-order modes, $m\pi x \ll W$ in the modulation region and, from Eq. (1) with a square modulation profile $\hat{\varepsilon}_1(x)$, a $\kappa_{mm} \sim m^2$ dependence is found as follows (we restrict ourselves to $m = m'$ for simplicity):

$$\int |E_m|^2 \hat{\varepsilon}_1(x)\mathrm{d}x \approx \hat{\varepsilon}_1^{\max}\int_0^{W_{\text{modul}}} E_0^2 \sin^2\left(\frac{m\pi}{W}x\right)\mathrm{d}x = \hat{\varepsilon}_1^{\max} E_0^2\left(\frac{m\pi}{W}\right)^2 \frac{W_{\text{modul}}^3}{3}, \tag{B1}$$

$$\Gamma(m) \equiv \Gamma_1(m,m) = \frac{\int |E_m|^2 \hat{\varepsilon}_1(x)\mathrm{d}x}{\int |E_m|^2 \mathrm{d}x} \propto \frac{m^2 W^{-2}}{W} = \frac{m^2}{W^3}. \tag{B2}$$

For higher-order modes, on the contrary, $mx \sim W$ and $\sin^2(m\pi x/W)$ averages to one half in the modulated region or slowly varies depending on its detail. Then, contradirectional coupling becomes nearly constant for a large number of adjacent branches. This constancy is also true for contradirectional coupling between higher-order modes of different order—$\kappa_{mm'}$ with $m \neq m'$—for which the integrand just involves $\sin[(m\pi/W)x]\sin[(m'\pi/W)x]$ with $m, m' \gg 1$, without major changes of the order of magnitude of mode interactions.

ACKNOWLEDGMENTS

H. Kurt acknowledges the financial support of the Institut d'Optique for his stay at the Institute as a postdoctoral research fellow.

REFERENCES AND NOTES

1. T. Tamir, *Guided Wave Optoelectronics* (Springer-Verlag, 1990).
2. L. A. Coldren and S. W. Corzine, *Diode Lasers and Photonic Integrated Circuits* (Wiley, 1995).
3. G. P. Agrawal and N. K. Dutta, *Semiconductor Lasers*, 2nd ed. (Van Nostrand Reinhold, 1993).
4. A. Yariv, "Coupled mode theory for guided wave optics," IEEE J. Quantum Electron. **9**, 919–933 (1973).
5. A. Yariv and M. Nakamura, "Periodic structures for integrated optics," IEEE J. Quantum Electron. **13**, 233–253 (1977).
6. E. Peral, A. Yariv, and L. Fellow, "Supermodes of grating-coupled multimode waveguides and application to mode conversion between copropagating modes mediated by backward Bragg scattering," J. Lightwave Technol. **17**, 942–947 (1999).
7. A. Yariv, *Quantum Electronics* (Wiley, 1989).
8. D. Marcuse, *Theory of Dielectric Optical Waveguides* (Academic, 1974).
9. H. Benisty, "Modal analysis of optical guides with two-dimensional photonic band-gap boundaries," J. Appl. Phys. **79**, 7483–7492 (1996).
10. B. Lombardet, L. A. Dunbar, R. Ferrini, and R. Houdré, "Fourier analysis of Bloch wave propagation in photonic crystals," J. Opt. Soc. Am. B **22**, 1179–1190 (2005).
11. J. D. Joannopoulos, R. D. Meade, and J. N. Winn, *Photonic Crystals: Molding the Flow of Light* (Princeton University Press, 1995).
12. S. Olivier, H. Benisty, C. Weisbuch, C. J. Smith, T. F. Krauss, and R. Houdré, "Coupled-mode theory and propagation losses in photonic crystal waveguides," Opt. Express **11**, 1490–1496 (2003).
13. S. Olivier, M. Rattier, H. Benisty, C. J. M. Smith, R. M. De La Rue, T. F. Krauss, U. Oesterle, R. Houdré, and C. Weisbuch, "Mini stopbands of a one-dimensional system: the channel waveguide in a two-dimensional photonic crystal," Phys. Rev. B **63**, 113311 (2001).
14. L. Martinelli, H. Benisty, O. Khayam, G. H. Duan, H. Heidrich, and K. Janiak, "Analysis and optimization of compact demultiplexer monitor based on photonic crystal waveguide," J. Lightwave Technol. **25**, 2385–2394 (2007).
15. J.-M. Lourtioz, H. Benisty, V. Berger, J. M. Gérard, D. Maystre, and A. Tchelnokov, *Photonic Crystals: Towards Nanoscale Photonic Devices* (Springer, 2005).
16. D. Rosenblatt, A. Sharon, and A. A. Friesem, "Resonant

grating waveguide structures," IEEE J. Quantum Electron. **33**, 2038–2059 (1997).
17. P. Ferrand, R. Romestain, and J. C. Vial, "Photonic band-gap properties of a porous silicon periodic planar waveguide," Phys. Rev. B **63**, 115106 (2001).
18. S. Albaledejo, J. J. Saenz, M. Lester, L. S. Froufe-Pérez, and A. Garcia-Martin, "Optical conductance of waveguides built into finite photonic crystals," Appl. Phys. Lett. **91**, 061107 (2007).
19. T. Baba, D. Mori, K. Inoshita, and Y. Kuroki, "Light localizations in photonic crystal line defect waveguides," IEEE J. Sel. Top. Quantum Electron. **10**, 484–491 (2004).
20. Y. A. Vlasov, M. O'Boyle, H. F. Hamman, and S. J. McNab, "Active control of slow light on a chip with photonic crystal waveguides," Nature **438**, 65–69 (2005).
21. S. Combrié, E. Weidner, A. De Rossi, S. Bansropun, S. Cassette, A. Talneau, and H. Benisty, "Detailed analysis by Fabry–Perot method of slab photonic crystal line-defect waveguides and cavities in aluminium-free material system," Opt. Express **14**, 7353–7361 (2006).
22. H. Gersen, T. J. Karle, J. P. Engelen, W. Bogaerts, J. P. Korterik, N. F. van Huslt, T. F. Krauss, and L. Kuipers, "Real-space observation of ultraslow light in photonic crystal waveguides," Phys. Rev. Lett. **94**, 073903 (2005).
23. M. D. Settle, R. J. P. Engelen, M. Salib, A. Michaeli, L. Kuipers, and T. F. Krauss, "Flatband slow light in photonic crystals featuring spatial pulse compression and terahertz bandwidth," Opt. Express **15**, 219–226 (2007).
24. H. Benisty, A. David, L. Martinelli, E. Viasnoff-Schwoob, C. Weisbuch, G.-H. Duan, K. Janiak, and H. Heidrich, "From modal control to spontaneous emission and gain in photonic crystal waveguides," Photonics Nanostruct. Fundam. Appl. **4**, 1–11 (2006).
25. E. Viasnoff-Schwoob, C. Weisbuch, H. Benisty, C. Cuisin, E. Derouin, O. Drisse, G.-H. Duan, L. Legouézigou, O. Legouézigou, F. Pommereau, S. Golka, H. Heidrich, H. J. Hensel, and K. Janiak, "Compact wavelength monitoring by lateral outcoupling in wedged photonic crystal multimode waveguides," Appl. Phys. Lett. **86**, 101107 (2005).
26. O. Khayam, C. Cambournac, H. Benisty, M. Ayre, H. Brenot, and G. H. Duan, "In-plane Littrow lasing of broad photonic crystal waveguides," Appl. Phys. Lett. **91**, 041111 (2007).
27. A. B. Greenwell, S. Booruang, and M. G. Moharam, "Multiple wavelength resonant grating at oblique incidence with broad angular acceptance," Opt. Express **15**, 8626–8638 (2007).
28. A. A. Sukhorukov, C. J. Handmer, C. Martijn de Sterke, and M. J. Steel, "Slow light with flat or offset band edges in few-mode fiber with two gratings," Opt. Express **15**, 17954–17959 (2007).
29. S. Somekh, E. Garmire, A. Yariv, H. L. Garvin, and R. G. Hunsperger, "Channel optical waveguide directional couplers," Appl. Phys. Lett. **22**, 46–47 (1973).
30. M. Ghulinyan, Z. Gaburro, D. S. Wiersma, and L. Pavesi, "Tuning of resonant Zener tunneling by vapor diffusion and condensation in porous optical superlattices," Phys. Rev. B **74**, 045118 (2006).
31. U. Peschel, T. Pertsch, and F. Lederer, "Optical Bloch oscillations in waveguide arrays," Opt. Lett. **23**, 1701–1703 (1998).
32. I. Vorobeichikh, E. Narevicius, G. Rosenblum, M. Orenstein, and N. Moiseyev, "Electromagnetic realization of orders-of-magnitude tunneling enhancement in a double well system," Phys. Rev. Lett. **90**, 176806 (2003).
33. T. Pertsch, U. Peschel, and F. Lederer, "All-optical switching in quadratically nonlinear waveguide arrays," Opt. Lett. **28**, 102–104 (2003).
34. E. Viasnoff-Schwoob, C. Weisbuch, H. Benisty, S. Olivier, R. Houdré, and C. J. M. Smith, "Spontaneous emission enhancement at a photonic wire miniband edge," Opt. Lett. **26**, 2113–2115 (2005).
35. We believe that the extent of slowdown in (k,ω) space is akin to the issue of the natural radius of Fabry–Perot modes ($r_{\mathrm{FP}} \sim \sqrt{\lambda \times \mathrm{thickness} \times \mathrm{finesse}}$), which is itself tightly related to Fresnel zones ($r \sim \sqrt{\lambda \times \mathrm{distance}}$), that is, to the generic quadratic transverse behavior of transverse phase lags off an unfolded reference path). We may, along the same line, conjecture that thickness tolerances would be similar to those of high-finesse Fabry–Perot resonators, demanding thickness variations of less than $\delta W = \lambda/2/\mathrm{finesse}$ but with a precise finesse definition depending on the frequency span and thus on the number of oscillations being exploited.